Editors' Suggestion

Near-Surface Electrical Characterization of Silicon Electronic Devices Using Focused keV-Range Ions

S.G. Robson,[1,*] P. Räcke,[2,3] A.M. Jakob,[1] N. Collins,[1] H.R. Firgau,[4] V. Schmitt,[4] V. Mourik,[4] A. Morello,[4] E. Mayes,[5] D. Spemann,[2,3] and D.N. Jamieson[1]

[1] *Centre for Quantum Computation and Communication Technology, School of Physics, University of Melbourne, Parkville, Victoria 3010, Australia*
[2] *Leibniz Institute of Surface Engineering (IOM), Permoserstr. 15, Leipzig D-04318, Germany*
[3] *Leibniz Joint Lab "Single Ion Implantation", Permoserstr. 15, Leipzig D-04318, Germany*
[4] *Centre for Quantum Computation and Communication Technology, School of Electrical Engineering and Telecommunications, UNSW Sydney, Sydney, New South Wales 2052, Australia*
[5] *RMIT Microscopy and Microanalysis Facility, RMIT University, Melbourne, Victoria 3001, Australia*

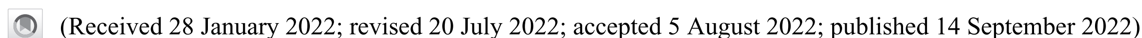
(Received 28 January 2022; revised 20 July 2022; accepted 5 August 2022; published 14 September 2022)

The demonstration of universal quantum logic operations near the fault-tolerance threshold has established ion-implanted near-surface donor atoms as a plausible platform for scalable quantum computing in silicon. The next technological step forward requires a deterministic fabrication method to create large-scale arrays of donors, featuring a few-hundred-nanometer interdonor spacing. Here, we explore the feasibility of this approach by implanting low-energy ions into silicon devices featuring a 60×60 μm^2 sensitive area and an ultrathin 3.2-nm gate oxide—capable of hosting large-scale donor arrays. We employ a characterization system consisting of a modified focused-ion-beam machine and ultralow-noise ion-detection electronics to demonstrate a method for evaluating the device response characteristics to shallowly implanted 12-keV $^{1}H_2^+$ ions. Despite the weak internal electric field, near-unity charge-collection efficiency is obtained from the entire sensitive area. This can be explained by the critical role that the thermal gate oxide plays in the ion-detection response, allowing an initial rapid diffusion of ion-induced charge away from the implant site. Next, we adapt our approach to perform deterministic implantation of a few thousand 24-keV $^{40}Ar^{2+}$ ions into a predefined microvolume, without any additional collimation. Despite the reduced ionization from the heavier ion species, a fluence-independent detection confidence of $\geq$99.99% is obtained. Our system thus represents not only a method for mapping the near-surface electrical landscape of electronic devices but also a framework toward mask-free prototyping of large-scale donor arrays in silicon.

DOI: 10.1103/PhysRevApplied.18.034037

I. INTRODUCTION

Devices based on complementary metal-oxide semiconductor (CMOS) technology, both in established applications for classical information technology and in emerging applications for quantum computing, depend on the precise control of electric fields in the near-surface region. In classical silicon transistors, the source-drain current flowing beneath a thin (<10-nm) gate oxide is modulated by the electric field from a surface gate [1]. The current flows in thin sheets, with the highest density closest to the Si-SiO_2 interface [2]. With the transistor size inside modern processors now approaching 5 nm [3], the concentration of fabrication defects on the nanoscale has become a critical issue. For example, local oxide thickness fluctuations, trapped interface charge, and atomic scale interface roughness can strongly affect the device internal electric field, leading to device reliability issues and breakdown [4,5]. In devices engineered for quantum applications, the electronic and nuclear spin of near-surface (<20-nm deep) donors in silicon can be used to encode information [6]. The quantum state of each atom is programmed and read out by electric fields from surface gates isolated from the substrate by a thin gate oxide [7]. Small-scale prototype devices have so far demonstrated nuclear coherence times exceeding 30 s [8], gate fidelities beyond 99.9% [9], and, more recently, universal quantum logic operations in a three-qubit processor with >99% fidelity [10]. To satisfy surface-code error-correction specifications, future quantum devices will require a large number ($>10^6$) of donors arranged in a near-surface array [7]. Besides being an

*simonr1@student.unimelb.edu.au

 © 2022 American Physical Society

enormous fabrication challenge in its own right, careful control of the internal electric field profile is critical for these devices to function correctly.

Among the possible fabrication pathways for incorporating near-surface donors in silicon, scanning probe lithography can be used to produce few-donor clusters [11] with subnanometer placement precision [12]. An alternative placement approach involves using low-energy ion implantation to produce well-separated individual donors. Already the industry standard for fabricating classical CMOS devices [13], we have recently extended this technique with the development of a deterministic ion-implantation system that uses the internal electric field within a silicon device to register stochastic arrival-time single-ion-implantation events [14]. The system has been used to demonstrate postimplant counted detection of a few thousand 14-keV P^+ ions in Si with 99.85% confidence, using an ion beam collimated to approximately 10 μm diameter by an *in situ* microstencil [14]. The inherent uncertainty of the final resting position of each ion in the silicon lattice furthermore meets the relaxed placement constraints of the "flip-flop" qubit architecture [7], where 100–500-nm interdonor spacing is permitted.

In this work, we investigate the possibility of enhancing this fabrication method to produce large-area arrays of single donors spanning tens of micrometers—a key prerequisite for a large-scale silicon quantum processor. The analysis is performed within an electronic device characterization system based on the focused ion beam (FIB), a well-understood analysis and fabrication technique that has been used within materials science for decades [15]. Typically incorporating a Ga liquid-metal ion source with an approximately 5-nm beam spot size, FIB can be used for milling microstructures in a variety of materials [16]. More recently, the use of light ion sources such as He and Ne has reduced the beam spot size to <0.5 nm [17], leading to applications in photonics [18] and quantum materials [19]. Using an updated generation of single-ion detectors that feature an ultrathin passivation gate oxide plus an enlarged sensitive area suitable for spin readout and control of donor arrays [7,14], we first scan a focused probe of 12-keV ${}^{1}H_2^+$ ions across the surface and measure the response of the device as a function of the beam position. This technique is commonplace for electrical-device characterization at few-micrometer depths using high-energy megaelectronvolt ions [20] but here we demonstrate its use in the low-kiloelectronvolt regime. As such, this provides a method to evaluate the near-surface (<100-nm) electronic properties. For devices that meet appropriate quality acceptance criteria, we then reconfigure the system to perform counted 24-keV ${}^{40}Ar^{2+}$ implants into the center of the sensitive region, without the use of an additional mask, and calculate the ion-detection confidence. This additionally allows us to assess the future suitability of employing the system to construct donor arrays in silicon.

II. METHODS

A. The modified FIB system

The experiments take place using a commercially available FIB machine (Raith ionLINE) that has been modified for this work [schematic shown in Fig 1(a)]. Full details of the machine are available in Ref. [21]. Briefly, the conventional liquid-metal ion source is replaced with an electron-beam ion source (EBIS) from DREEBIT GmbH [22]. This is a versatile high-brightness gas-plasma source that can produce ions in multiple charge states $q = \{1, 2, \ldots\}$ up to complete ionization [23]. In this study, Ar^{q+}- and H_2^+-molecular ions are employed. The base pressure in the ion source chamber is kept below 10^{-9} mbar. The source potential can vary between 3 and 20 kV but is generally set to 12 kV for these experiments, resulting in a kinetic ion-implantation energy of $E = q \times 12$ keV. Mass and charge-state selection occur via an integrated Wien filter, with a retractable Faraday cup located at the source output for ion-beam diagnostics. The ion-focusing optics are comprised of objective and condenser apertures ranging from 1 to 200 μm in size, selectable via an electrically driven aperture stage. An octupole stigmator ensures a circular ion-beam profile. The beam is demagnified by the FIB lens system and can be scanned across the sample stage using the integrated high-speed pattern generator. The working distance is 10 mm. Additionally, the interferometrically controlled sample stage can be positioned to <2-nm accuracy across its entire 200-mm travel range and provides an alternative precision sample-stepping method. Coarse lateral ion-beam alignment (approximately 10 μm) is accomplished by an optical camera, whilst secondary electron imaging via an integrated Everhart-Thornley detector enables precision sample alignment to within approximately 20 nm. Beam currents between 0.1 and 100 ion/s are achieved by combining direct-filament current control and Wien-filter detuning.

B. Single-ion detection

The ion beam is focused onto a custom-fabricated silicon diode (referred to hereafter as a detector) mounted on an integrated preamplifer printed circuit board. The assembly is housed within a metal case [see Fig. 1(b)] that is fixed to the FIB sample stage. The detector design incorporates a localized p-doped top-electrode region and a uniform n-doped back contact in 520-μm-thick uniform high-purity [001] float zone Si (n-type, 9250 Ω cm) to form a vertical "sandwich-type" p-i-n structure, as shown in Figs. 1(c)–1(f). The electrodes are metallized with 200-nm-thick Al to form Ohmic contacts for wire bonding. Ions are designed to be implanted into the center of the detector (region A, referred to hereafter as the "construction site," CS), which is covered by a thermally grown passivation gate oxide of between 3- and 6-nm nominal thickness.

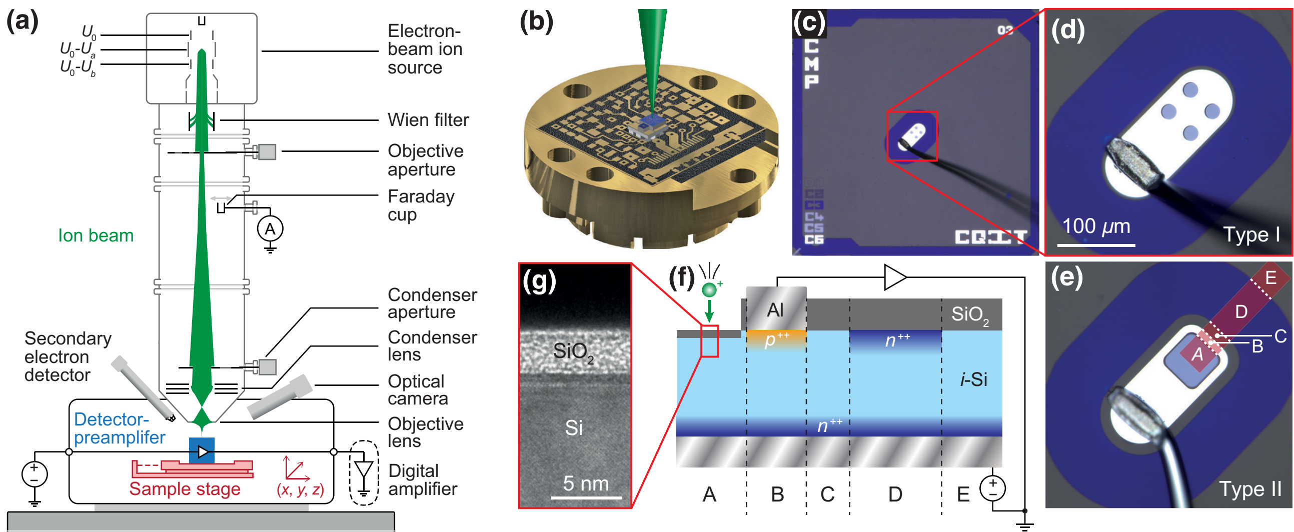

FIG. 1. (a) A schematic of the FIB machine, equipped with an electron-beam-ion-source and integrated single-ion-detection electronics mounted on a precision sample stage. The ion-beam profile is based on an actual ray-tracing simulation [21]. (b) A computer-aided-design image of the single-ion-detection setup. It consists of a preamplifier circuit board housed in a metal case of 4 cm diameter. The ion beam (green) is focused onto an on-chip silicon *p*-*i*-*n* diode detector that is directly connected to a low-noise junction field-effect transistor (JFET). Both the detector and the JFET are mounted on a thermoelectric cooling element at the center of the board. (c) An optical micrograph showing the top-view layout of the ion-detector diode. Two different layouts of (d) (4×20 μm)-diameter construction sites (CSs) or (e) one central 60×60 μm^2 CS are available. (f) A cross-section schematic of the detector [as indicated in (e)], showing the "sandwich-type" *p*-*i*-*n* diode structure. The gate oxide inside the CS is between 3 and 6 nm thick, while the surrounding field oxide exhibits approximately 65 nm thickness. The aluminum electrodes are approximately 200 nm thick. (g) A representative cross-section transmission-electron-microscope image of the CS of a detector.

The remainder of the detector surface is covered by a thermally grown field oxide of approximately 65-nm thickness [regions C, D, and E in Fig. 1(f)]. The top electrode (region B) is surrounded by a buried floating *n*-doped guard ring (region D) to screen against excess leakage current from interface and bulk-defect states in the surrounding region [24]. Two detector models are studied in this work: a previous generation incorporating four circular CSs, each with 20-μm diameter and having a 5.9-nm-thick gate oxide ["Type I," Fig. 1(d)]; and a new generation utilizing a single CS of 60-μm edge length ["Type II," Fig. 1(e)] with either a 5.2-nm- or 3.2-nm-thick gate oxide. Full details on the general detector design and fabrication process are described elsewhere [14]. The key properties of the specific detectors employed in this work are summarized in Table I.

Each ion-impact event is measured using the ion-beam-induced-charge (IBIC) technique [25]. As each ion strikes the detector, a cascade of electron-hole (*e*-*h*) pairs is created along its deceleration trajectory. The number of *e*-*h* pairs produced in the sensitive silicon-detection volume n_0 is proportional to the remaining kinetic ion energy after passing through the oxide passivation "dead" layer $E' = E - \delta E$ and is made up of contributions from the primary ion as well as those of respective recoiled target atoms. Through a process of diffusion and drift (from the internal electric field or with an additional external reverse bias), the *e*-*h* pairs become separated. A fraction may recombine at trapping sites in the silicon bulk as well as at the Si-SiO_2 interface, resulting in $n < n_0$ *e*-*h* pairs reaching the electrodes. By connecting the detector to a charge-sensitive preamplifier circuit, the electrical impulse due to ion-induced charge movement toward the electrodes can be measured. The ion-detection ability of the detector is typically quantified by the charge-collection efficiency $\eta = n/n_0$.

In this work, an ultralow-noise preamplifier based on the design of Bertuccio *et al.* [26] is employed. It incorporates

TABLE I. A summary of the individual properties of each detector used in this work.

Detector name	Wafer ID	Gate oxide thickness (nm)	Field oxide thickness (nm)	CS type
A-1	A	5.2[a]	62	II
B-1	B	5.9	65	I
C-1	C	3.2	68	II
C-2	C	3.2	68	II

[a]An additional 500-nm-thick layer of SU-8 resist is deposited on the gate oxide and formed into a calibration pattern via electron-beam lithography.

a forward-biased junction field-effect transistor (JFET) [27], which, together with the detector, is mounted on an integrated thermoelectric cooling element [see Fig. 1(b)]. The detector is operated under reverse bias by applying +10 V to the lower electrode and connecting the top electrode to the JFET gate via a wire bond. Further signal processing occurs entirely within the integrated preamplifier. Modest cooling to -10°C is applied during operation, resulting in a typical root-mean-square (rms) noise of approximately 70 eV [14]. The preamplified signal output is then fed into an Amptek PX5 digital-pulse processor [28], which performs trapezoidal pulse shaping ($\tau = 9.6\ \mu$s peaking time), amplification, and digitization. Channel-to-energy conversion is accomplished by comparing the ion response against that of a ^{57}Co calibration radionuclide that emits characteristic Fe 6.40-keV K_{α} and 7.06-keV K_{β} X-ray photons. The correlation between the known ion-beam position (provided directly from the FIB pattern generator) and the detected signal from each ion impact is realized using a custom-written NI LabVIEW program.

III. RESULTS AND DISCUSSION

A. Setup characterization

1. FIB performance

Evaluation of the ion-beam profile takes place with detector A-1, where an additional 500 nm of SU-8 resist is deposited on the surface and selectively developed into a calibration pattern using electron-beam lithography. A checkerboard layout with pitch size ranging from 4 to 0.5 μm is formed inside the CS, as shown in Fig. 2(a). The detector is subsequently placed inside the FIB machine, where a 6-keV $^{1}H_2^+$ beam is then scanned over a $10 \times 10\ \mu m^2$ area inside the CS. Light ions are employed for the initial characterization because they produce less sample damage and greater ionization than heavier species for the same kinetic energy [20]. Each $^{1}H_2^+$ molecule ion dissociates quasi-instantaneously upon surface impact, due to the energy transfer exceeding the binding energy by several orders of magnitude [29]. The constituent ions share the total kinetic energy in equal parts (3 keV per H^+) and decelerate simultaneously inside the detector. Ions that strike areas protected by the resist cannot produce signal pulses, as its thickness is large enough to prevent incident ions from entering the sensitive detector volume [30]. In resist-free areas, the average penetration depth is approximately 47 nm below the Si-SiO_2 interface and a combined sum of 1560 *e*-*h* pairs (subject to Poisson statistics) is produced per H_2^+ ion [30]. The shallow implantation depth compared to the overall detector thickness causes the IBIC signal pulse to be dominated by electron drift toward the back electrode, whereas holes contribute to only a minor degree [31].

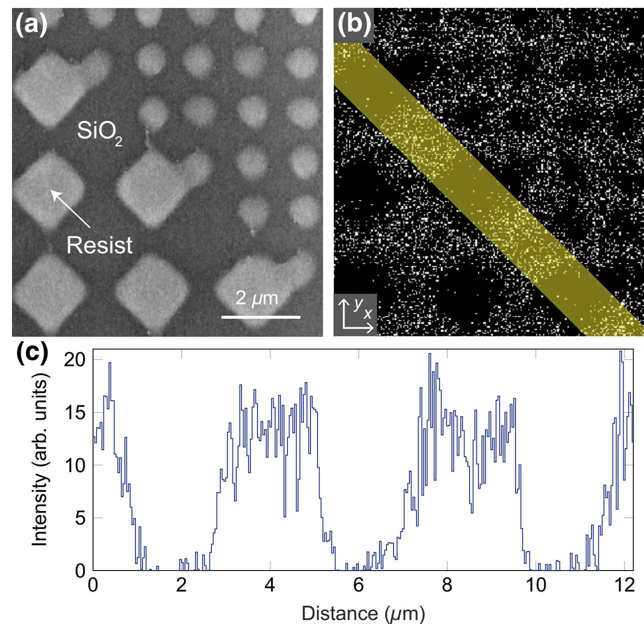

FIG. 2. (a) A secondary electron image taken inside the CS of detector A-1, showing the checkerboard pattern formed by a 500-nm-thick SU-8 resist layer deposited on the gate oxide. Squares of 2 μm and 1 μm pitch can be seen. (b) The corresponding 256×256 pixel spatially resolved single-ion-impact event map, created by a focused beam of 6 keV H_2^+ ions. A total of 6521 ion impacts are recorded, with each white pixel corresponding to a single detected ion-impact event. The ion-impact rate is approximately 20 ion/s and the dwell time is fixed at 8 ms. The objective and condenser aperture sizes are set to 1 μm and 10 μm, respectively. (c) A line scan extracted from the yellow-shaded line in (b) and integrated over its width.

Figure 2(b) demonstrates a spatially resolved map of the ion-induced signal events captured with optimized FIB column parameters. A comparison against the actual calibration pattern visualized via scanning electron microscopy [Fig. 2(a)] shows that the overall shape appears to be well reproduced by the system. The majority of detected ion-impact events originate from resist-free areas and the pattern aspect ratio is preserved, indicating optimized ion-beam stigmator settings. However, some residual scattered events are also seen to occur within resist-covered areas. To better understand this finding, intensity line profiles are extracted from the ion-impact event map, with an example shown in Fig. 2(c). The left-hand edge of each plateau [with respect to Fig. 2(c)] appears to have a consistently greater spread than the right-hand edge, with this highly directional behavior indicating unwanted residual FIB coma effects. This can be addressed by further fine adjustment of the ion optical alignment [21]. The beam spot of the system is thus determined by fitting an error function to the unaffected right-hand edge. An average full width at half maximum (FWHM) of 181 ± 14 nm is obtained along an extended

edge feature. This is a substantial improvement over other EBIS-based FIB machines, where values of between 500 and 1000 nm have been reported [23,32,33]. However, this does not represent the lower-resolution limit of this system. An even smaller spot size can be obtained by further reducing the FIB aperture size to below 100 nm—ion-induced-event maps can be still be generated in a matter of minutes, despite the predicted < 1-fA beam current. Custom-fabricated nanoapertures are currently under evaluation for this purpose [34].

2. Ion-energy measurement and mapping

To confirm correct operation of the system, a 12-keV $^{1}H_2^+$ ion beam is scanned over a detector with a previously measured response to similar-energy $^{1}H_2^+$ ions [14] (detector B-1, type I) and the signal-pulse amplitudes are recorded. In the absence of incident ions, a rms noise of approximately 110 eV is measured. This is about 40 eV greater than other detectors from the same wafer [14] and can be attributed to an additional capacitance at the JFET input gate from a second detector that is connected in parallel during this experiment. However, this is sufficient for high-confidence low-energy single-ion detection, as discussed later. A total of 10 000 single-ion-impact events are recorded, with the resulting signal-pulse spectrum shown in Fig. 3(a). The spectrum is dominated by a broad main peak centered at 2.5 keV, with a fraction of its lower-energy side cut off due to the noise-discriminator threshold. On the high-energy side, a separate small signal peak occurs at 5.8 keV and approximately 700-eV FWHM. One further isolated small peak, centered at 11.3 keV and approximately 600-eV FWHM, can also be identified.

The corresponding spatially resolved charge-signal-pulse map is shown in Fig. 3(b) and reveals the origin of each peak. Each pixel is color coded according to the charge-collection efficiency η determined from the pulse recorded at the given location. The overall map features agree well with the optical top-view micrograph of the same device shown in Fig. 1(d). As expected, the isolated highest-energy signal peak originates inside the CS array [region A in Fig. 1(f)]. Here, the initial ion-energy loss from stopping in the thin gate oxide (see Table I) is negligible. The known low-defect concentrations found in the silicon bulk and at the thermal-gate-oxide interface [14,35] maximize the number of *e*-*h* pairs produced in the sensitive volume, resulting in $\eta \approx 1$. For a 12-keV H_2^+ molecule ion, approximately 95% of its kinetic energy is dissipated in electronic stopping by *e*-*h*–pair generation according to the model of Funsten and Ziegler [30,36]. With the signal-peak center located at approximately 11.3 keV, our results are consistent with this model and also with previous experimental results obtained with a collimated beam from a conventional plasma-filament ion source [14], thus confirming the correct functionality of the system. Additional

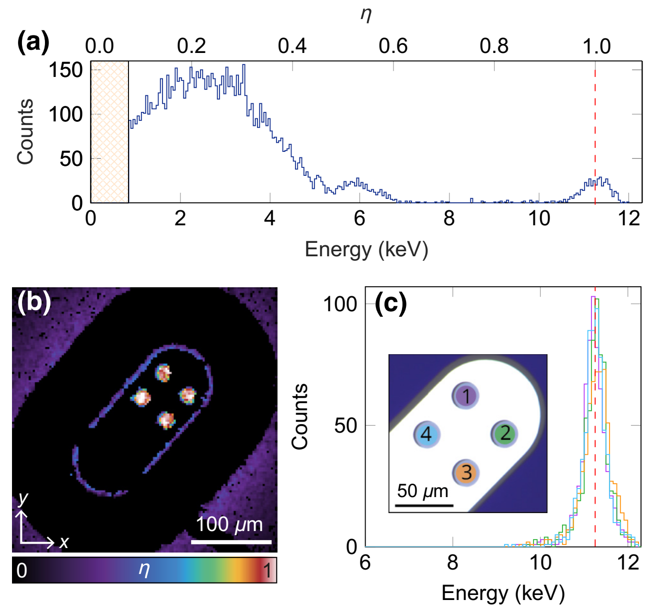

FIG. 3. (a) A signal-pulse spectrum of detector B-1 exposed to a scanned 12-keV H_2^+ beam. The three peaks correspond to different regions of the device with varying η, as discussed in the text. The hatched interval [0, 0.84] keV indicates the noise-discriminator regime. The red dashed line indicates an average charge-collection efficiency of $\langle\eta\rangle = 1$. (b) A spatially resolved 128 × 128 pixel map of the data presented in (a). The dark strip extending to the bottom-right corner is due to the shadowing effect of the 20-μm-thick wire bond attached to the metal top electrode. (c) Signal-pulse spectra extracted from detailed scans performed inside each CS (as indicated in each highlighted area in the inset optical image). Each spectrum is comprised of approximately 650 single-ion-impact events.

spectra obtained from independently scanning each individual CS are also shown in Fig. 3(c). There appears to be minimal variation in η between each CS and the absence of isolated events outside the main signal peak indicates negligible artificial influences—e.g., from ion scattering or gate-oxide effects such as thickness fluctuations and surface debris.

Outside the CS array, the top metal electrode pad (region B) yields no single-ion-detection events, agreeing with TRIM simulations that predict that 100% of 12 keV H_2^+ molecule ions should stop completely within the metal layer [30]. Next, the narrow undoped region between the top electrode and the *n*-doped guard ring (region C) gives rise to the satellite signal peak located at 6 keV. Here, the ions experience increased stopping in the thicker field oxide (see Table I) and lose approximately half of their initial kinetic energy before reaching the sensitive detector volume [30]. Hence, only approximately half the number of *e*-*h* pairs is generated in this region, compared to in region A. Further, no signal events are recorded within the *n*-doped guard-ring area (region D) due to the very high

phosphorous doping concentration (3×10^{19} cm^{-3}), representing a volume of very effective *e*-*h*–pair recombination.

Finally, the outer area (region E) yields the dominant signal peak in Fig. 3(a), with the peak size coming from its relatively large-area fraction of the detector. Here, the *n*-guard ring strongly attenuates the internal reverse-bias drift field, rendering the slower charge-carrier diffusion process (minority-carrier lifetimes typically approximately 100 ns, compared to picosecond drift times [37]) as the dominant transport mechanism. The spatially isotropic nature of *e*-*h*–pair diffusion, combined with lifetime-limiting interface and bulk defects, results in a quick decline of η with growing lateral distance from the *n*-doped guard edge. However, we emphasize that ions are not actually designed to be implanted and detected in this region. Instead, the earlier result showing $\eta \to 1$ within each CS (region A) is the key conclusion to draw from this initial experiment.

B. Defect measurement and analysis

Turning to our application to silicon donor-based quantum computing, we now evaluate type-II detectors incorporating a large-area CS needed to host large-scale donor arrays. We test the key array-formation requirement: all implanted ions must be able to be detected with a high degree of confidence at their predefined target locations. More precisely, η must meet two criteria in the CS: (1) the average value must be near-unity, and (2) it must be spatially homogeneous. As previously introduced, the IBIC technique is inherently sensitive to defects located in the bulk [39,40] and at interfaces [41,42], which act as trapping or recombination centers for ion-induced free *e*-*h* pairs. Especially for criterion (2), local effects such as gate-oxide thickness fluctuations or residual nanoscale surface debris can contribute toward increased ion stopping before an ion reaches the sensitive detector volume, leading to highly localized areas of reduced η. This cannot be readily evaluated with broad-beam ion implantation and, instead, a scanned focused-ion microprobe must be used. Furthermore, low-kinetic-energy kiloelectronvolt ions are needed (unlike in conventional megaelectronvolt IBIC experiments [20]) to ensure that a similar depth scale to that used for eventual donor-array ion implants is probed.

To evaluate the presence of such defects, two representative detectors from the same fabrication wafer [see Figs. 4(a) and 4(b)] are selected at random and mapped with a scanned 12-keV H_2^+ beam. Figure 4(c) shows a high-resolution map of η in detector C-1. The CS exhibits ideal signal characteristics and clearly fulfills both criteria. A line scan taken diagonally along its cross section [Fig. 4(e)] confirms fluctuations in η of $<3\%$. These can be attributed to the statistical nature of a multiatom collision cascade that each ion experiences, due to (i) variations in the residual kinetic ion energy after transmitting the gate oxide, (ii) variations in the electronic ion stopping fraction in the sensitive region, and (iii) the Fano statistics of *e*-*h*–pair generation due to electron and hole scattering in the silicon lattice [43]. This is also the origin of the signal-peak width visible in Fig. 3(c). The sharp decrease in η at the CS perimeter is due to an abrupt transition between the gate oxide and the thicker surrounding field oxide.

The situation is markedly different for detector C-2. As shown in Figs. 4(d) and 4(e), three distinct regions of different η are observable within the CS. The right-hand third (region I) exhibits comparably uniform signal characteristics with near-unity η, similar to detector C-1. However, the remaining regions indicate the presence of defects. Two pockets of degraded $\eta < 0.5$ occur at the top and in the center of the CS (region II). They span approximately 10×20 μm in lateral dimensions. In the left-hand third of the CS (region III), a more uniform spatial detector response is apparent, albeit with a reduced average $\eta \approx 0.9$. To better understand the charge-collection dynamics, a COMSOL® simulation [38] of the electric field **E** inside an ideal ($\eta = 1$) detector is run, with the results shown in Fig. 4(f). **E** is largely uniform and vertically aligned deep inside the detector but increasingly realigns horizontally in the vicinity of the surface. This is accompanied by a lateral gradient in the absolute field strength, with a near-field-free region existing in the center of the CS to a depth of a few micrometers. This is many times the ion-implantation depth (88 ± 30 nm [30]), suggesting that in this region, the motion of ion-generated free *e*-*h* pairs is initially characterized by diffusion and later becomes dominated by drift transport in the deeper silicon bulk. The conclusion is that a Si crystal with few point or extended defects [see Fig. 1(g)] and a well-passivated surface from a thermally grown oxide [44] appears sufficient to create an environment with diffusion lengths spanning tens of micrometers, as exhibited by detector C-1. This is clearly not the case in detector C-2.

The shallow ion-probing depth suggests that the physical origin of the defective regions in detector C-2 may be surface related. Atomic force microscopy is thus performed in the affected area of the CS, as indicated in Fig. 4(d). The corresponding topography map is shown in Fig. 4(g). A hairline crack extending from the top corner to the center of the CS can be identified, with lateral dimensions varying between a few hundred nanometers and a few micrometers. In some areas, the crack has a depth of up to 4 nm. This is comparable to the thermal-gate-oxide thickness, suggesting that an error during the fabrication process (e.g., residual surface debris present during spin coating or a mechanical scratch from wafer handling) results in its local etching. The complete removal of a thermally grown oxide and subsequent exposure of the underlying silicon material leads to the formation of a native oxide (2–3 nm thickness), typically characterized by defect-interface trap densities $D_{\mathrm{it}} > 10^{13}$ cm^{-2} eV^{-1} and

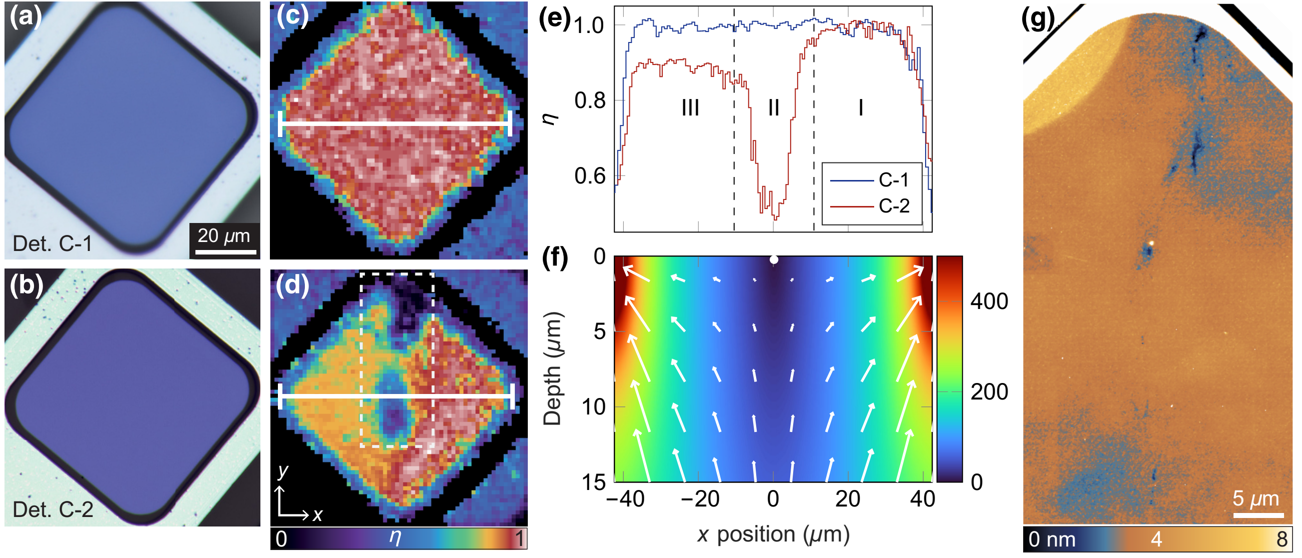

FIG. 4. 100× optical micrographs showing the CSs of (a) detector C-1 and (b) detector C-2. (c),(d) Corresponding spatially resolved 256 × 256 pixel signal-pulse maps captured using a scanned 12-keV H_2^+ beam with an approximately 20-ion/s incidence rate and a fixed 8-ms dwell time. A two-pixel binning algorithm is applied to compensate for some void pixels. (e) Line profiles of η, extracted along the horizontal diagonal (x axis) of the CS of each detector [indicated by white lines in (c) and (d)]. Regions of similar η for detector C-2 are indicated and discussed in the text. (f) A COMSOL® simulation [38] showing the strength and direction of the internal electric field **E** (V cm^{-1}) inside an ideal detector, taken along the same cross section as in (e). An external reverse bias of −10 V is applied. Peak doping concentrations of 1×10^{16} cm^{-2} are specified in the p and n Ohmic contact regions against a 1×10^{11} cm^{-2} n-type background. An interface defect density of $D_{it} = 1 \times 10^{11}$ cm^{-2} eV^{-1} and a fixed oxide charge of $Q_f = 1 \times 10^9$ cm^{-2} are assumed in the gate oxide. The white dot at the image center indicates the expected average implantation depth of 12-keV H_2^+ ions according to TRIM calculations [30]. (g) The topography map of detector C-2 obtained with atomic force microscopy. The scan area is indicated by the dashed white rectangle in (d).

fixed-oxide charge densities $Q_f > 10^{12}$ cm^{-2} [45]. These values lie several orders of magnitude higher than those measured in a typical thermal gate oxide [35,46], thus representing a concentrated region of effective e-h–pair trapping and recombination. The corresponding signal-pulse map [Fig. 4(d)] clearly reflects a reduced charge-carrier lifetime in and around this damaged region, where only 20–50% of the ion-induced e-h pairs are collected at the detector electrodes.

The nonuniform ion-detection response exhibited by detector C-2 therefore makes this device unsuited to hosting a large-scale donor array, demonstrating the crucial need for a low-interface-density passivation thermal oxide in donor-based silicon quantum computing applications. However, this appears to be an isolated case, with other detectors from the same wafer also tested (not shown) and confirmed to be fit for purpose. Moreover, these results demonstrate the importance of using application-relevant low-energy kiloelectronvolt ions in the initial device characterization, in order to understand and troubleshoot the device behavior at the near surface. The versatility of this system should also be pointed out in allowing not only analysis of silicon-based electronic devices but potentially those based on other IBIC-compatible platforms, such as SiC, diamond, and III–V materials [20].

C. Mask-free deterministic ion implantation

We now turn our attention toward reconfiguring the setup to enable future controlled implantation of individual $^{31}P^+$ ions for use in spin-based quantum computing. In these experiments, 24-keV $^{40}Ar^{2+}$ ions (acceleration potential = 12 kV) are employed. Each ion penetrates 28 ± 13 nm below the Si-SiO_2 interface and generates an average of approximately 1700 e-h pairs in the active detection volume [30]. Although the electronic and spin properties of ^{40}Ar do not make it compatible with quantum information processing in silicon, its ion-stopping characteristics are very similar to those of the ^{31}P donor qubit [48], providing a good estimate of the ion-detection signal response and thus allowing a robust assessment of further adapting the FIB setup for this ultimate purpose.

In a large-scale quantum computing device incorporating surface control gates [7,49], it is important to minimize the depth-placement uncertainty (longitudinal straggle) of each donor. Too deep placement results in poor spin-dependent tunnel coupling of the donor electron, whereas too shallow placement causes the donor to be located adjacent to or in the oxide and consequently inactivated. The straggle can be reduced by lowering the implantation energy (see Table II). However, this also reduces the

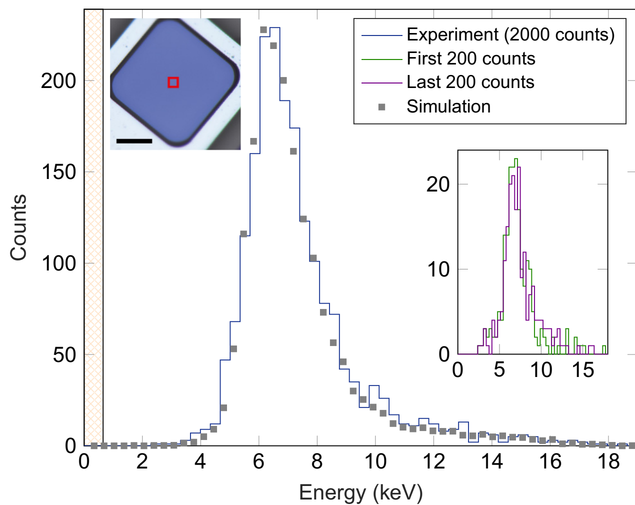

FIG. 5. A signal-pulse spectrum of detector C-1 irradiated with a focused beam of 2000 24-keV Ar^{2+} ions, raster scanned over a 5×5 μm^2 area inside the CS (as indicated in the left inset; scale bar = 20 μm). The dwell time is set to 1 ms and the incidence rate is approximately 10 ion/s. The low-level discriminator is set to 640 eV, corresponding to the hatched region. Also shown are the results of normalized Crystal-TRIM simulations [47] of the same experiment, performed with 20 000 ions. The right inset shows subspectra from the first and last 200 recorded counts.

number of ion-induced *e-h* pairs and thus causes the amplitude of each charge pulse signal to lie near the noise threshold, thereby increasing the likelihood of >1 donor per implant site. The net result is a reduced ensemble coherence time from uncontrolled nearby donor-donor coupling. The solution is to reach an optimum balance between the placement uncertainty and the ion-detection confidence $\Xi(q_{t0})$, defined as the fraction of detected single-ion events (counts above the noise-discriminator threshold q_{t0}) to the total number of incident ions [14]. To predict $\Xi(q_{t0})$, a 5×5 μm^2 area located at the center of the CS (left inset of Fig. 5) in detector C-1 is continuously scanned with a 24 keV Ar^{2+} beam until 2000 signal events are recorded. The resulting signal-pulse spectrum is shown in Fig. 5. Compared to $^{1}H^{+}$, the heavier mass of $^{40}Ar^{2+}$ results in only 25% of the initial ion kinetic energy being dissipated into electronic stopping [36], shifting the peak centroid down to approximately 6.1 keV. The peak also appears broader due to a greater statistical variation in the fraction of electronic energy loss of each ion. Nevertheless, a clear interval between the lowest detected count (at 2.5 keV) and the noise-discrimination threshold (at 0.64 keV) lacking any signal events is seen, strongly suggesting that 100% of the incident ions are successfully detected.

A robust assessment of $\Xi(q_{t0})$ is done by comparing the experimentally obtained signal-pulse spectrum with that generated by a Crystal-TRIM simulation [47] for an ideal ($\eta = 1$) silicon detector with the same gate-oxide thickness. Good agreement between the experimental and simulated spectra is observed, allowing us to extract a detection confidence of $\Xi(q_{t0}) \geq 99.99\%$. The effect of the accumulated ion fluence on the signal-pulse spectrum [50] is additionally considered by comparing the first and last 200 detected events, as shown in the right inset of Fig. 5. Within the statistical uncertainty of the two subspectra, no evidence of a systematic peak shift or broadening is seen, suggesting that even moderate ion-induced crystal damage (an average Ar^{2+} interion spacing of 112 nm—almost 4 times the intended donor density for the chosen quantum device architecture [7]) does not lead to a significant degradation in η.

Compared to previous detector generations incorporating a standard 6–8-nm gate oxide [14], detector C-1 features an ultrathin 3.2-nm gate oxide [see Fig. 1(g)] from optimization of the oxide growth process. Similar CMOS devices incorporating sub-5-nm gate oxides have been shown to be susceptible to elevated defect concentrations [51]. However, the near-unity η value obtained here suggests that the density of interface defect traps and fixed oxide charge within this ultrathin gate oxide is in fact comparable to that measured in previous-generation devices [8,10]. A thin gate oxide also provides an improved controlled silicon doping yield Y_{dop}, defined as the fraction of detectable single-ion impacts where the primary dopant ion also entirely transmits the gate oxide to stop inside the silicon crystal. Events where the primary ion stops inside the oxide may still produce a detectable signal, because forward-recoiled Si and O atoms from the oxide can also contribute to an overall charge-signal-pulse event. These events appear to be extremely rare for this detector generation, with Crystal-TRIM simulations [47] predicting $Y_{dop} = 99.95\%$ for 24-keV Ar^{2+} ions. Using a type-I detector, we have previously reported a single-ion-detection confidence of $\Xi(q_{t0}) = 99.85\%$ for 14-keV $^{31}P^{+}$ ions but the actual doping yield has been limited to $Y_{dop} = 98.1\%$, due to 1.9% of the incident $^{31}P^{+}$ ions stopping inside the 6-nm gate oxide [14]. Extrapolating the present results obtained with Ar ions, we expect a factor-of-5 enhancement to $Y_{dop} = 99.62\%$ for 14-keV $^{31}P^{+}$ ions when implanted into type-II detector, comfortably exceeding the latest estimates of tolerable donor-qubit-loss fault thresholds (90%–95%) [52]. The production of $^{31}P^{+}$ ions from an EBIS has already been demonstrated [53] and is currently forthcoming in our setup.

The lateral placement accuracy of each implanted ion is the additional component in determining the suitability of our setup for scalable donor-array fabrication in silicon and can be split into two independent scattering processes. First, the uncertainty of the lateral impact point of each ion on the detector surface comes from the fixed spot size of the FIB. Second, lateral ion straggling takes place inside the target material (see Table II) as a direct result of the

TABLE II. The properties of selected ion species (and in some cases, varied kinetic energies) when implanted through a 3.2-nm-thick SiO_2 layer into (100) Si, as modeled by Crystal-TRIM [47]. The implantation depth is calculated from the Si-SiO_2 interface. The number of *e-h* pairs is calculated in the sensitive detection volume, with a 640-eV noise floor assumed to determine the ion-detection confidence. Starred entries (*) denote results that have not yet been experimentally verified.

Species	E_{kin} (keV)	Implantation depth ± straggle (nm)	Lateral straggle (nm)	n_0 (*e-h* pairs)	$\Xi(q_{t0})$ (%)	Y_{dop} (%)
$^{1}H_2^+$	12	86.9 ± 31.2	40.3	3112	≥99.99	99.91
$^{40}Ar^{3+}$	36	40.3 ± 17.6	14.4	2764	≥99.99	99.99
$^{40}Ar^{2+}$	24	27.8 ± 13.0	10.6	1695	≥99.99	99.95
$^{40}Ar^{+}$	12	14.6 ± 7.8	6.3	625	99.84	99.68
$^{31}P^{+}$	14	19.7 ± 10.7	9	1108	99.98*	99.62*
$^{31}P^{+}$	9	12.9 ± 7.7	6.5	643	99.85*	98.98*

random collision cascade that each ion makes with target atoms upon stopping. Although the present 181-nm (FWHM) spot size is not compatible with the sub-50-nm lateral-donor-placement constraints of the flip-flop qubit architecture [7], we expect a further spot-size reduction to <30 nm to be realistically achievable by employing custom-fabricated 100-nm-diameter lens apertures [34], as mentioned earlier. In this regime, effects from the spot size and the lateral ion straggling in silicon should contribute more or less equally to the overall ion-placement precision. Furthermore, the expected reduction in beam current from the smaller aperture size can be offset by the highly adjustable nature of the EBIS emission intensity, yielding a similar expected on-target implantation rate to that used in the present experiments. Precision localization of single ions has already been demonstrated with a masked approach, where a nanoaperture has been milled in the tip of an atomic-force-microscope cantilever and placed directly above the sample to collimate the beam [54]. However, adapting this technique below the 30-nm level may be technically challenging due to expected lateral and axial ion straggling effects from the aperture. Particularly for high-aspect-ratio nanoapertures, an unacceptably large proportion of ions can be implanted hundreds of nanometers away from their intended target locations [55]. This effect can also be aggravated by the accumulated ion fluence seen by the cantilever, whereby the nanoaperture can shrink and eventually completely close over time [54,56]. The use of a maskless focused implantation method, such as the FIB system employed in this work, may present a viable avenue around this.

Our system also has the advantage that highly charged ions (up to completely ionized) can readily be supplied by the EBIS. Especially for heavy donors such as ^{123}Sb and ^{209}Bi, the additional potential energy deposited by these ions in the detector [57] may result in an increased $\Xi(q_{t0})$. Alongside recent studies from systems that detect single in-flight ions just prior to the implantation event [58,59], our results represent a pathway toward the scalable engineering of near-surface donor-qubit arrays with nanoscale placement precision.

IV. CONCLUSIONS

We introduce an electronic device characterization system that uses a FIB equipped with an electron-beam ion source as well as ultralow-noise single-ion-detection technology to enable deterministic control over the number and position of implanted ions. The highly adjustable source can produce ions with energies between 3 and 300 keV, implanted at rates between 0.1 and 100 ion/s, focused down to a spot size of 180 nm (FWHM). Through the IBIC principle, we use silicon *p-i-n* diode detectors to measure *e-h* pairs generated by each ion-impact event and correlate this with the beam position. Using an updated generation of ion detectors featuring an enlarged 60×60 μm^2 sensitive area and an ultrathin 3.2-nm gate oxide, we first spatially map the internal electric field to within 100 nm of the surface using a rastered 12-keV $^{1}H_2^+$ ion probe. The results highlight the destructive effect that localized regions of defect-rich native oxide have in suppressing the detection response, whereby >50% of the initially diffused charge can be lost to associated interface states. Nevertheless, near-unity charge-collection efficiency is measured in the sensitive area of functional detectors, thus confirming that our devices are fit for purpose. Next, we modify the system to perform counted implantation of 2000 $^{40}Ar^{2+}$ ions at 24 keV into a predefined 5×5 μm^2 area, obtaining ≥99.99% single-ion-detection confidence. This approach foregoes the need for a mechanical implant mask that may introduce additional ion scattering. With an upcoming system upgrade to incorporate a $^{31}P^{+}$ ion source and yield a sub-30-nm FIB spot size, we aim to establish a viable method to fabricate large-scale near-surface ^{31}P donor arrays in silicon for multiqubit entanglement studies.

ACKNOWLEDGMENTS

This work was funded by the Australian Research Council Centre of Excellence for Quantum Computation and Communication Technology (Grant No. CE170100012) and the U.S. Army Research Office (Contract No. W911NF-17-1-0200). This work was performed in part in the NSW Node of the Australian National Fabrication

Facility at the UNSW Sydney. S.G.R., P.R., and A.M.J. acknowledge an Australia-Germany Joint Research Cooperation Scheme (UA-DAAD) travel scholarship that supported collaboration between partner institutions. S.G.R. acknowledges additional travel support from the Laby Foundation Pty Ltd. S.G.R., N.C., and H.R.F. acknowledge support from an Australian Government Research Training Program Scholarship. P.R. and D.S. gratefully acknowledge funding by the Leibniz Association (SAW-2015-IOM-1) and the European Union, together with the Sächsisches Ministerium für Wissenschaft und Kunst (Project No. 100308873). The code for the Crystal-TRIM simulations performed in this work was developed by M. Posselt of Helmholtz-Zentrum Dresden-Rossendorf. The authors acknowledge the facilities, and the scientific and technical assistance, of the RMIT Microscopy & Microanalysis Research Facility at RMIT University as well as the assistance of J. Bauer and of A. Finzel, both of the Leipzig Institute of Surface Engineering (IOM), the former for performing additional electron microscopy and the latter for performing atomic force microscopy. The views and conclusions contained in this document are those of the authors and should not be interpreted as representing the official policies, either expressed or implied, of the Army Research Office or the U.S. Government. The U.S. Government is authorized to reproduce and distribute reprints for government purposes notwithstanding any copyright notation herein.

[1] S. M. Sze, *Semiconductor Devices: Physics and Technology* (John Wiley & Sons, New York, 2012), 3rd ed.

[2] W. D. Rau, P. Schwander, F. H. Baumann, W. Höppner, and A. Ourmazd, Two-Dimensional Mapping of the Electrostatic Potential in Transistors by Electron Holography, Phys. Rev. Lett. **82**, 2614 (1999).

[3] IEEE, International Roadmap for Devices and Systems (2021).

[4] A. Asenov, S. Kaya, and J. H. Davies, Intrinsic threshold voltage fluctuations in decanano MOSFETs due to local oxide thickness variations, IEEE Trans. Electron Devices **49**, 112 (2002).

[5] A. Asenov, A. R. Brown, J. H. Davies, S. Kaya, and G. Slavcheva, Simulation of intrinsic parameter fluctuations in decananometer and nanometer-scale MOSFETs, IEEE Trans. Electron Devices **50**, 1837 (2003) .

[6] B. E. Kane, A silicon-based nuclear spin quantum computer, Nature **393**, 133 (1998).

[7] G. Tosi, F. A. Mohiyaddin, V. Schmitt, S. Tenberg, R. Rahman, G. Klimeck, and A. Morello, Silicon quantum processor with robust long-distance qubit couplings, Nat. Commun. **8**, 450 (2017).

[8] J. T. Muhonen, J. P. Dehollain, A. Laucht, F. E. Hudson, R. Kalra, T. Sekiguchi, K. M. Itoh, D. N. Jamieson, J. C. McCallum, A. S. Dzurak, and A. Morello, Storing quantum information for 30 seconds in a nanoelectronic device, Nat. Nanotechnol. **9**, 986 (2014) .

[9] J. P. Dehollain, J. T. Muhonen, R. Blume-Kohout, K. M. Rudinger, J. K. Gamble, E. Nielsen, A. Laucht, S. Simmons, R. Kalra, A. S. Dzurak, and A. Morello, Optimization of a solid-state electron spin qubit using gate set tomography, New J. Phys. **18**, 103018 (2016).

[10] M. T. Mądzik, S. Asaad, A. Youssry, B. Joecker, K. M. Rudinger, E. Nielsen, K. C. Young, T. J. Proctor, A. D. Baczewski, A. Laucht, V. Schmitt, F. E. Hudson, K. M. Itoh, A. M. Jakob, B. C. Johnson, D. N. Jamieson, A. S. Dzurak, C. Ferrie, R. Blume-Kohout, and A. Morello, Precision tomography of a three-qubit donor quantum processor in silicon, Nature **601**, 348 (2022).

[11] J. A. Ivie, Q. Campbell, J. C. Koepke, M. I. Brickson, P. A. Schultz, R. P. Muller, A. M. Mounce, D. R. Ward, M. S. Carroll, E. Bussmann, A. D. Baczewski, and S. Misra, Impact of Incorporation Kinetics on Device Fabrication with Atomic Precision, Phys. Rev. Appl. **16**, 054037 (2021).

[12] L. Fricke, S. J. Hile, L. Kranz, Y. Chung, Y. He, P. Pakkiam, M. G. House, J. G. Keizer, and M. Y. Simmons, Coherent control of a donor-molecule electron spin qubit in silicon, Nat. Commun. **12**, 3323 (2021).

[13] J. M. Poate and K. Saadatmand, Ion beam technologies in the semiconductor world (plenary), Rev. Sci. Instrum. **73**, 868 (2002).

[14] A. M. Jakob, S. G. Robson, V. Schmitt, V. Mourik, M. Posselt, D. Spemann, B. C. Johnson, H. R. Firgau, E. Mayes, J. C. McCallum, A. Morello, and D. N. Jamieson, Deterministic shallow dopant implantation in silicon with detection confidence upper-bound to 99.85% by ion-solid interactions, Adv. Mater. **34**, 2103235 (2022).

[15] J. Orloff, High-resolution focused ion beams, Rev. Sci. Instrum. **64**, 1105 (1993).

[16] P. Li, S. Chen, H. Dai, Z. Yang, Z. Chen, Y. Wang, Y. Chen, W. Peng, W. Shan, and H. Duan, Recent advances in focused ion beam nanofabrication for nanostructures and devices: Fundamentals and applications, Nanoscale **13**, 1529 (2021).

[17] N. Klingner, G. Hlawacek, P. Mazarov, W. Pilz, F. Meyer, and L. Bischoff, Imaging and milling resolution of light ion beams from helium ion microscopy and FIBs driven by liquid metal alloy ion sources, Beilstein J. Nanotechnol. **11**, 1742 (2020).

[18] M. Manoccio, M. Esposito, A. Passaseo, M. Cuscunà, and V. Tasco, Focused ion beam processing for 3D chiral photonics nanostructures, Micromachines **12**, 6 (2020).

[19] P. J. Moll, Focused ion beam microstructuring of quantum matter, Annu. Rev. Condens. Matter Phys. **9**, 147 (2018).

[20] E. Vittone, Semiconductor characterization by scanning ion beam induced charge (IBIC) microscopy, ISRN Mater. Sci. **2013**, 1 (2013).

[21] P. Räcke, R. Wunderlich, J. W. Gerlach, J. Meijer, and D. Spemann, Nanoscale ion implantation using focussed highly charged ions, New J. Phys. **22**, 083028 (2020).

[22] M. Schmidt, H. Peng, G. Zschornack, and S. Sykora, A compact electron beam ion source with integrated Wien filter providing mass and charge state separated beams of highly charged ions, Rev. Sci. Instrum. **80**, 063301 (2009).

[23] F. Ullmann, F. Großmann, V. P. Ovsyannikov, J. Gierak, and G. Zschornack, Production of a helium beam in a focused ion beam machine using an electron beam ion trap, Appl. Phys. Lett. **90**, 083112 (2007).

[24] L. Evensen, A. Hanneborg, B. S. Avset, and M. Nese, Guard ring design for high voltage operation of silicon detectors, Nucl. Instrum. Methods Phys. Res. Sect. A: Accelerators, Spectrometers, Detectors Associated Equipment **337**, 44 (1993).

[25] M. B. Breese, E. Vittone, G. Vizkelethy, and P. J. Sellin, A review of ion beam induced charge microscopy, Nucl. Instrum. Methods Phys. Res. Sect. B: Beam Interactions Materials Atoms **264**, 345 (2007).

[26] G. Bertuccio and A. Pullia, Room temperature x-ray spectroscopy with a silicon diode detector and an ultra low noise preamplifier, IEEE. Trans. Nucl. Sci. **41**, 1704 (1994).

[27] Moxtek Inc., N-Channel Ultra-low Noise JFETs Catalog (2004).

[28] Amptek Inc., A250 Charge Sensitive Preamplifer Datasheet (2017).

[29] R. Cooks, T. Ast, and M. Mabud, Collisions of polyatomic ions with surfaces, Int. J. Mass Spectrom. Ion Process. **100**, 209 (1990).

[30] J. F. Ziegler, M. D. Ziegler, and J. P. Biersack, SRIM—The stopping and range of ions in matter (2010), Nucl. Instrum. Methods Phys. Res., Sect. B: Beam Interactions Materials Atoms **268**, 1818 (2010).

[31] E. Vittone, Z. Pastuovic, P. Olivero, C. Manfredotti, M. Jaksic, A. Lo Giudice, F. Fizzotti, and E. Colombo, Semiconductor characterization by scanning ion beam induced charge (IBIC) microscopy, Nucl. Instrum. Methods Phys. Res., Sect. B: Beam Interactions Materials Atoms **266**, 1312 (2008).

[32] S. Guillous, C. Bourin, B. Ban D'Etat, A. Benyagoub, A. Cassimi, C. Feierstein, E. Gardés, E. Giglio, S. Girard, C. Grygiel, A. Houel, H. Lebius, A. Méry, I. Monnet, J.-M. Ramillon, J. Rangama, F. Ropars, E. Verzeroli, M. Viteau, and A. Delobbe, A new setup for localized implantation and live-characterization of keV energy multiply charged ions at the nanoscale, Rev. Sci. Instrum. **87**, 113901 (2016).

[33] M. Schmidt, P.-F. Laux, J. Gierak, and G. Zschornack, *AIP Conference Proceedings 2011*, (2018), p. 090027 https://doi.org/10.1063/1.5053408.

[34] D. Emmrich, A. Beyer, A. Nadzeyka, S. Bauerdick, J. C. Meyer, J. Kotakoski, and A. Gölzhäuser, Nanopore fabrication and characterization by helium ion microscopy, Appl. Phys. Lett. **108**, 163103 (2016).

[35] B. Johnson, J. McCallum, L. Willems van Beveren, and E. Gauja, Deep level transient spectroscopy study for the development of ion-implanted silicon field-effect transistors for spin-dependent transport, Thin Solid Films **518**, 2524 (2010).

[36] H. Funsten, S. Ritzau, R. Harper, and R. Korde, Response of 100% internal carrier collection efficiency silicon photodiodes to low-energy ions, IEEE Trans. Nucl. Sci. **48**, 1785 (2001).

[37] M. B. Breese, A theory of ion beam induced charge collection, J. Appl. Phys. **74**, 3789 (1993).

[38] COMSOL AB, www.comsol.com COMSOL Multiphysics® v5.6 (2020).

[39] E. C. Auden, J. L. Pacheco, E. Bielejec, G. Vizkelethy, J. B. Abraham, and B. L. Doyle, Sub-micron resolution of localized ion beam induced charge reduction in silicon detectors damaged by heavy ions, IEEE Trans. Nucl. Sci. **62**, 2919 (2015).

[40] E. Vittone, Z. Pastuovic, M. B. Breese, J. Garcia Lopez, M. Jaksic, J. Raisanen, R. Siegele, A. Simon, and G. Vizkelethy, Charge collection efficiency degradation induced by MeV ions in semiconductor devices: Model and experiment, Nucl. Instrum. Methods Phys. Res., Sect. B: Beam Interactions Materials Atoms **372**, 128 (2016).

[41] G. Vizkelethy, D. K. Brice, and B. L. Doyle, Heavy ion beam induced current/charge (IBIC) through insulating oxides, Nucl. Instrum. Methods Phys. Res. Sect. B: Beam Interactions Materials Atoms **249**, 204 (2006).

[42] A. M. Tonigan, D. Ball, G. Vizkelethy, J. Black, D. Black, J. Trippe, E. Bielejec, M. L. Alles, R. Reed, and R. D. Schrimpf, Impact of surface recombination on single-event charge collection in an SOI technology, IEEE Trans. Nucl. Sci. **68**, 305 (2021).

[43] E. Steinbauer, P. Bauer, M. Geretschläger, G. Bortels, J. Biersack, and P. Burger, Energy resolution of silicon detectors: Approaching the physical limit, Nucl. Instrum. Methods Phys. Res. Sect. B: Beam Interactions Materials Atoms **85**, 642 (1994).

[44] D. M. Fleetwood, P. S. Winokur, R. A. Reber, T. L. Meisenheimer, J. R. Schwank, M. R. Shaneyfelt, and L. C. Riewe, Effects of oxide traps, interface traps, and "border traps" on metal-oxide-semiconductor devices, J. Appl. Phys. **73**, 5058 (1993).

[45] T. Hori, *Gate Dielectrics and MOS ULSIs* (Springer-Verlag, Berlin, Berlin, 1997), 1st ed., p. 1.

[46] J. J. Pla, K. Y. Tan, J. P. Dehollain, W. H. Lim, J. J. L. Morton, D. N. Jamieson, A. S. Dzurak, and A. Morello, A single-atom electron spin qubit in silicon, Nature **489**, 541 (2012).

[47] M. Posselt and J. Biersack, Computer simulation of ion implantation into crystalline targets, Nucl. Instrum. Methods Phys. Res. Sect. B: Beam Interactions Materials Atoms **64**, 706 (1992).

[48] T. Hopf, C. Yang, S. E. Andresen, and D. N. Jamieson, The response of silicon detectors to low-energy ion implantation, J. Phys.: Condens. Matter **20**, 415205 (2008).

[49] C. D. Hill, E. Peretz, S. J. Hile, M. G. House, M. Fuechsle, S. Rogge, M. Y. Simmons, and L. C. L. Hollenberg, A surface code quantum computer in silicon, Sci. Adv. **1**, e1500707 (2015).

[50] A. Simon, G. Kalinka, M. Jaksic, Z. Pastuovic, M. Novak, and A. Kiss, Investigation of radiation damage in a Si PIN photodiode for particle detection, Nucl. Instrum. Methods Phys. Res. Sect. B: Beam Interactions Materials Atoms **260**, 304 (2007).

[51] J. H. Stathis and D. J. DiMaria, in *International Electron Devices Meeting 1998, Technical Digest* (Cat. No. 98CH3 6217), 1998, p. 167, https://doi.org/10.1109/IEDM.1998.746309.

[52] S. Nagayama, A. G. Fowler, D. Horsman, S. J. Devitt, and R. V. Meter, Surface code error correction on a defective lattice, New J. Phys. **19**, 023050 (2017).

[53] U. Kentsch, S. Landgraf, M. Schmidt, H. Tyrroff, G. Zschornack, F. Grossmann, V. P. Ovsyannikov, and F. Ullmann, Slow highly charged ions for nanoscale surface modifications, Nucl. Instrum. Methods Phys. Res., Sect. B: Beam Interactions Materials Atoms **216**, 196 (2004).

[54] S. Pezzagna, D. Wildanger, P. Mazarov, A. D. Wieck, Y. Sarov, I. Rangelow, B. Naydenov, F. Jelezko, S. W. Hell, and J. Meijer, Nanoscale engineering and optical addressing of single spins in diamond, Small **6**, 2117 (2010).

[55] N. Raatz, C. Scheuner, S. Pezzagna, and J. Meijer, Investigation of ion channeling and scattering for single-ion implantation with high spatial resolution, Physica Status Solidi (a) **216**, 1900528 (2019).

[56] J. Li, D. Stein, C. McMullan, D. Branton, M. J. Aziz, and J. A. Golovchenko, Ion-beam sculpting at nanometre length scales, Nature **412**, 166 (2001).

[57] T. Schenkel, A. V. Barnes, T. R. Niedermayr, M. Hattass, M. W. Newman, G. A. Machicoane, J. W. Mc Donald, A. V. Hamza, and D. H. Schneider, Deposition of Potential Energy in Solids by Slow, Highly Charged Ions, Phys. Rev. Lett. **83**, 4273 (1999).

[58] P. Räcke, D. Spemann, J. W. Gerlach, B. Rauschenbach, and J. Meijer, Detection of small bunches of ions using image charges, Sci. Rep. **8**, 9781 (2018).

[59] C. Lopez, A. Trimeche, D. Comparat, and Y. Picard, Real-Time Trajectory Control of Deterministically Produced Ions, Phys. Rev. Appl. **11**, 064049 (2019).